Max-Min Fairness in Active Aerial Reconfigurable Intelligent Surface-aided ISAC Network

Shanza Shakoor, *Student Member, IEEE,* Quang Nhat Le, *Member, IEEE,* Long D. Nguyen, *Member, IEEE,*
Keshav Singh, *Member, IEEE,* Octavia A. Dobre, *Fellow, IEEE,* and Trung Q. Duong, *Fellow, IEEE*

Abstract—This paper considers an unmanned aerial vehicle (UAV)-assisted sensing and communication framework that integrates an active reconfigurable intelligent surface (RIS). We aim at maximizing the sum of the minimum signal-to-interference-plus-noise ratios (SINRs) of user equipments within the whole integrated sensing and communication period by coordinating the optimization of several components: the transmit beamforming matrix and receive filter at a base station serving dual roles in radar and communication, the reflection coefficients of the active RIS mounted on the UAV, and the UAV's trajectory. The non-convexity of the objective function, combined with the intricate dependencies among variables, makes the problem highly complex. To address these complexities, a novel alternating optimization approach is introduced, combining techniques such as generalized Rayleigh quotient optimization, semidefinite relaxation, majorization-minimization methods, and sequential quadratic programming. Numerical experiments validate the proposed method, showing substantial SINR improvements compared to benchmark solutions that use fixed UAV trajectories, active RIS, passive RIS, or randomly configured phase shifts.

Index Terms—max-min fairness, reconfigurable intelligent surface (RIS), unmanned aerial vehicle (UAV), active RIS, integrated sensing and communication (ISAC).

I. INTRODUCTION

As we move towards the next frontier in wireless communication, sixth generation (6G) networks are expected to revolutionize how we connect, interact, and communicate. With the anticipated demands for robust, low-latency communication, widespread connectivity, and improved sensing capabilities, 6G requires the integration of multiple technologies that can seamlessly support both communication and sensing within a unified framework [1], [2]. This concept is encapsulated in integrated sensing and communication (ISAC),

S. Shakoor, Q. N. Le, and O. A. Dobre are with Memorial University, St. John's, NL A1C 5S7, Canada (e-mail: {sshakoor, qnle, odobre}@mun.ca).

Keshav Singh is with the Institute of Communication Engineering, National Sun Yat-sen University, Kaohsiung 80424, Taiwan (e-mail: keshav.singh@mail.nsysu.edu.tw).

L. D. Nguyen is with Duy Tan University, Da Nang 550000, Vietnam (email: nguyendinhlong1@duytan.edu.vn).

T. Q. Duong is with Memorial University, St. John's, NL A1C 5S7, Canada, and also with Queen's University Belfast, BT7 1NN Belfast, U.K (e-mail: tduong@mun.ca).

where wireless systems not only transmit data but also simultaneously sense their environment, enabling a variety of cutting-edge applications including autonomous systems, real-time situational awareness, and intelligent environments. By merging communication and sensing in a single network, ISAC systems promise to optimize spectrum usage, reduce hardware complexity, and unlock new paradigms in wireless connectivity [3], [4].

A critical enabler for ISAC systems is reconfigurable intelligent surface (RIS) which plays a pivotal role in advancing wireless communication systems through two distinct yet complementary functions [5], [6]. Firstly, RIS dynamically optimizes the channel's scattering environment, mitigating multipath interference and significantly improving the system's multiplexing gain [7], [8]. Secondly, RIS possesses the ability to precisely steer the propagation of signals and coherently combine their in-phase components within a three-dimensional space, thereby dramatically enhancing the intensity of the received signals [9]. This dual functionality enables RIS to elevate communication performance to new heights, particularly in complex propagation scenarios [10]. In ISAC, passive RIS can significantly enhance the reliability of both communication and environmental sensing, as demonstrated in [11], where, by modifying the phase and reflective properties of signals, RIS can enable better detection and localization, making it an indispensable component for achieving efficient communication and accurate environmental sensing. Similarly, the study in [12] introduced an advanced optimization algorithm to improve multi-target detection and multi-user communication performance by using passive RIS.

In addition to RIS, unmanned aerial vehicles (UAVs) have gained significant attention as versatile mobile platforms capable of enhancing wireless coverage and network adaptability [13], [14]. When integrated with RIS, UAVs transform into agile relay stations that can dynamically adjust the wireless channel from an aerial vantage point [15]–[17]. This combination of UAVs and RIS enables the network to respond in real-time to fluctuations in the wireless environment, addressing challenges such as signal blockage, interference, and coverage gaps. The integration of RIS-carrying UAVs within an ISAC framework can adjust beam patterns and control radio wave propagation in real-time, supporting the ISAC framework by offering a powerful solution to optimize both network performance and user fairness, thus ensuring seamless communication even in complex or rapidly changing network conditions. For instance, the authors of [18] designed an energy-efficient mobile edge computing (MEC) system

supported by aerial RIS, to boost energy efficiency by refining the UAV's flight path and RIS beamforming strategies.

Active RIS extends the concept of passive RIS by incorporating active elements, allowing for more sophisticated and adaptable manipulation of the electromagnetic environment. Unlike passive RIS which only reflects signals, active RIS can both amplify and reflect signals, offering enhanced control over channel conditions. Although passive RIS is recognized for its energy-efficient operation and its capability to manipulate electromagnetic waves without active signal amplification, the effectiveness of passive RIS is inherently limited by the double path loss effect, making it challenging to achieve substantial performance gains without resorting to large-scale RIS configurations [19], [20]. In contrast, active RIS overcomes these challenges by providing signal amplification, resulting in enhanced coverage, better signal strength, and more efficient resource utilization. Recent studies in [21] and [22] highlight the remarkable benefits of employing active RIS in ISAC systems, including improved data throughput, better network reliability, and enhanced sensing accuracy.

By integrating active RIS with UAVs and leveraging the synergy between communication and sensing, our work explores the performance of max-min fairness in an active aerial RIS (ARIS)-aided ISAC network. The objective is to ensure fair performance by boosting the lowest SINR experienced by user equipment (UEs) while enhancing both communication and sensing capabilities. Through the combination of active RIS, UAV, and ISAC, this work aims to provide insights into the potential of this advanced network paradigm for future wireless communications.

A. Related Work

The rapid evolution of ISAC systems, coupled with the deployment of RIS, is transforming modern wireless networks, particularly in enhancing signal quality and resource efficiency [23]. RIS uses programmable meta-atoms to adjust the phase and direction of reflected electromagnetic waves. RIS is commonly classified into two main types: passive RIS which reflects signals, and active RIS which amplifies and reflects signals, are both utilized to improve performance, especially in challenging environments [19], [20].

Numerous studies have explored the use of RIS in fixed infrastructures like walls or rooftops to reflect and steer signals towards users. For instance, the authors in [24] and [25] demonstrated that passive RIS has shown its potential in improving signal strength, minimizing power consumption, and extending coverage, especially in high path-loss or interference areas. Furthermore, the authors in [26] showed that employing passive RIS can help optimize downlink communication and radar performance, minimizing multi-user interference (MUI) in ISAC systems. Another investigation in [27] examined how RIS supports wireless networks in secure scenarios, optimizing the service quality for standard UEs while ensuring a secure rate for confidential UEs and minimizing the transmit power of the base station (BS). However, passive RIS has certain limitations, including its inability to amplify signals, limiting its effectiveness in dynamic or high path-loss environments.

To address this, active RIS has been explored as an efficient solution. Active RIS can enhance throughput and reliability by compensating for weak signals and reducing interference [21]. In [28], the authors proposed a unified framework combining transmit precoding at the BS and active RIS beamforming. Their approach aimed to optimize both parameter estimation accuracy and signal-to-interference-plus-noise ratio (SINR) performance by employing an alternating optimization strategy grounded in semidefinite relaxation (SDR) and majorization-minimization (MM) techniques. Similarly, the study in [29] explored how fairness can be achieved in ISAC systems through the integration of simultaneous transmitting and reflecting RIS and non-orthogonal multiple access, effectively mitigating interference.

The concept of mounting RIS on UAVs has garnered attention due to its mobility and flexibility. Specifically, passive RIS mounted on UAVs can dynamically optimize signal reflection based on UE locations and environmental conditions. For example, the authors in [18] investigated UAV-mounted RIS systems for MEC, aiming to enhance energy efficiency through the strategic adjustment of RIS phase configurations and the optimization of UAV's trajectory. In [30], the authors focused on maximizing the aggregate data rate for ground users by strategically optimizing UAV positioning, configuring the RIS phase shifts, and allocating sub-channels efficiently. Similarly, the authors in [31] concentrated on achieving max-min throughput for mobile vehicles by coordinating RIS phase adjustments, scheduling strategies, UAV's trajectory, and BS's power allocation. These efforts are foundational for achieving fair resource distribution and optimizing system performance, which align with the objective of max-min fairness. In [32], UAV-mounted RIS systems were employed to optimize line-of-sight (LoS) conectivity between BSs and UEs by minimizing UAV requirements and enhancing overall network performance by minimizing the number of needed UAVs, which is a step toward optimizing network efficiency. The active nature of these systems allows for greater control over the signal propagation, resulting in optimal spectrum utilization and higher communication performance. However, the complexity of implementing active components and the increased power consumption of such systems remain key challenges for practical deployment.

In recent years, research has expanded to explore the potential of active RIS mounted on UAVs. ARIS has the advantage of dynamic signal amplification and reconfiguration, which can greatly improve the network coverage in high path-loss areas and ensure better performance for UEs with poor signal conditions. The authors in [33] proposed a secure communication framework using an ARIS, which integrates sensing, positioning, and power beamforming to protect privacy information against mobile eavesdropper. In summary, while recent studies have explored UAV-mounted RIS systems for enhancing wireless communication and sensing in ISAC networks, the literature on this topic remains limited. Existing research primarily focuses on optimizing UAV placement, RIS's phase shifts, and beamforming to improve signal quality, coverage, and resource efficiency. However, an important open issue is the need for further investigation into the role of

ARIS in these systems, particularly in achieving fairness and enabling dynamic adaptation to changing environments.

B. Motivations and Contributions

In [22], authors aimed to optimize radar SINR by refining both the beamforming matrix at the dual-functional radar and communication BS (DFRC-BS) and the reflection parameters of the active RIS. Similarly, [21] proposed a joint optimization strategy involving the transmit beamformer, active RIS reflection matrix, and radar receive filter in ISAC systems. Their proposed algorithm effectively enhanced radar output signal-to-noise ratio (SNR), showcasing notable performance gains. Although these works focus on maximizing the SNR or SINR for radar and communication UEs, they do not directly address the user fairness problem, which remains a key challenge in practical deployment. Moreover, these studies typically assume fixed RIS configurations, neglecting the dynamic potential offered by mobile RIS platforms like UAVs.

This paper investigates max-min SINR optimization for communication UEs in an ISAC system with UAV-mounted active RIS. The key focus of our work is to maximize the sum of minimum SINRs of the worst-performing UEs within the whole ISAC period, ensuring equitable service across all UEs while satisfying radar quality requirements. Our approach jointly optimizes the beamforming matrix and the receive filter at the BS, along with the reflection coefficient matrix at the ARIS, while also adhering to the power constraints at both the BS and ARIS. Unlike prior works that target SNR for the radar, we prioritize ensuring a minimum SINR for communication UEs, which is crucial for guaranteeing fairness in multi-user systems. The contributions of this work are outlined below:

- We address the challenge of maximizing the sum of minimum SINRs for communication UEs within the whole ISAC period in the ISAC system supported by an active RIS mounted on a UAV. The optimization involves the joint design of the BS's transmit beamforming and receive filter, the configuration of the active RIS's amplification and phase adjustments, and determining the UAV's trajectory, while ensuring compliance with power limits, SINR requirements for users and radar targets, and UAV's trajectory.

- An efficient alternating optimization (AO) algorithm is proposed to solve the non-convex optimization problem by leveraging the generalized Rayleigh quotient optimization, SDR, MM framework, and sequential quadratic programming (SQP) for the joint design of the receive filter and transmit beamforming of the BS, amplification and phase shift matrix of the active RIS, and the UAV's trajectory.

- Simulation results confirm the swift convergence of the proposed approach and highlight a substantial enhancement in minimum SINR, surpassing baseline methods with fixed UAV trajectories, passive RIS, or arbitrary phase shift configurations.

The paper is organized as follows: Section II presents the system model, and Section III outlines the formulation of the max-min SINR problem fo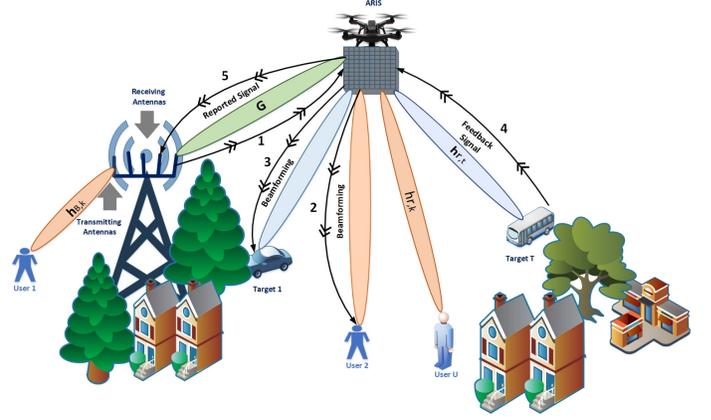r communication UEs. Section IV introduces the proposed AO algorithm designed to address the optimization challenge. Numerical results evaluating the performance of the AO algorithm are discussed in Section V. Finally, section VI concludes the paper.

Fig. 1. Active RIS-mounted UAV-aided ISAC system model.

C. Notations

Vectors and matrices are denoted by bold lowercase and uppercase letters, respectively. The space of $N \times 1$ complex-valued vectors is represented as $\mathbb{C}^{N \times 1}$, while $\mathbb{C}^{N \times M}$ represents the set of $N \times M$ complex-valued matrices. The Hermitian transpose, trace, and rank of a matrix $\mathbf{W}$ are denoted by $\mathbf{W}^H$, $\mathrm{Tr}(\mathbf{W})$, and $\mathrm{Rank}(\mathbf{W})$, respectively. A matrix $\mathbf{W}$ is positive semidefinite if $\mathbf{W} \succeq 0$. The expectation operation is represented as $\mathbb{E}[\cdot]$, and $\mathrm{diag}(\phi)$ creates a diagonal matrix with the elements of vector ϕ on its diagonal. The Euclidean norm of $\mathbf{w}$ is written as $\|\mathbf{w}\|$, while $\mathbf{I}_N$ denotes the $N \times N$ identity matrix. The magnitude of a complex number a is represented by $|a|$.

II. SYSTEM MODEL

Fig. 1 depicts the proposed active RIS-mounted UAV-aided ISAC system model. The system comprises a DFRC-BS, equipped with $\mathcal{M} = \{1, \dots, M\}$ number of transmitting/receiving antennas, serving $\mathcal{K} = \{1, \dots, K\}$ UEs each equipped with a single antenna, while concurrently performing a single target detection. We assume that the communication UEs have both LoS and non LoS connections, whereas the direct path between the DFRC-BS and the target is assumed unavailable. To boost system performance, the ARIS facilitates communication when LoS connections between the BS and UEs or the target are obstructed. In particular, the ARIS consists of N elements, indexed by $\mathcal{N} = \{1, \dots, N\}$ and is supported by an additional power source. We assume that the ARIS operates in a 2D plane at a fixed altitude, starting from an initial location $\mathbf{q}_{t,i} = [x_i, y_i]$. The ISAC period, denoted by T_0, is evenly divided into T discrete time slots, each with a fixed duration η, i.e., $T_0 = T\eta$. At time slot t, the UAV's position is denoted by $\mathbf{q}_t = [x_t, y_t]$. Furthermore, we also assume that UAV flies within the specified area $\mathcal{X} \times \mathcal{Y}$, which is as follows:

$$\mathbf{q}_t \in \mathcal{X} \times \mathcal{Y}, \quad \forall t \in \{1, 2, \dots, T\}. \tag{1}$$

Due to the limited velocity of the ARIS, the velocity is subject to

$$\|\mathbf{q}_t - \mathbf{q}_{t-1}\| \le \eta \upsilon_{\max}, \quad \forall t = \{2, \ldots, T\}, \tag{2}$$

where υ_{max} represents the maximum permissible velocity of the ARIS. The propulsion energy consumed by the ARIS during flight depends on its speed, acceleration, and flight duration. The flight energy consumption of ARIS at time slot t can be modeled as [34]–[36]

$$\mathcal{E}_t^{\text{ARIS}} = \left(P_0 \left[1 + \frac{3\upsilon_t^2}{U_{\text{tip}}^2} \right] + P_1 \left(\sqrt{1 + \frac{\upsilon_t^4}{4\upsilon_0^4} - \frac{\upsilon_t^2}{2\upsilon_0^2}} \right)^{\frac{1}{2}} + \wp \upsilon_t^3 \right) \eta, \tag{3}$$

where $P_0, P_1, U_{\text{tip}}, \upsilon_0,$ and $\wp$ are constants related to the ARIS aerodynamics, υ_t is the speed of the ARIS, $\upsilon_t = \frac{\|\mathbf{q}_t - \mathbf{q}_{t-1}\|}{\eta}$. Standard parameter values in (3) are listed in Table I [37].

TABLE I
STANDARD PARAMETER VALUES FOR (3)

Parameter	Value
P_0	80 W
U_{tip}	120 m/s
υ_0	4 m/s
υ_{max}	20 m/s
P_1	31.43 W
$\wp$	0.0046 kg/m

The transmitted signal at time slot t is represented by $\mathbf{x}_t \in \mathbb{C}^{M \times 1}$, and it can be mathematically expressed as a superposition of the beamformed sensing and communication components

$$\mathbf{x}_t = \underbrace{\mathbf{W}_{k,t} s_{k,t}}_{\text{Communications signal}} + \underbrace{\mathbf{W}_{s,t} s_{s,t}}_{\text{Radar signal}} = \mathbf{W}_t s_t,$$

where $s_{k,t} \in \mathbb{C}^{K \times 1}$ and $s_{s,t} \in \mathbb{C}^{M \times 1}$ represent the transmitted communication and sensing symbols, respectively. Furthermore, $\mathbf{W}_{k,t} \in \mathbb{C}^{M \times K}$ and $\mathbf{W}_{s,t} \in \mathbb{C}^{M \times M}$ are the transmit beamforming and sensing matrices at time slot t, respectively. The transmit signal can be represented by its covariance matrix, defined as

$$\mathbf{R}(\mathbf{W}_t) = \mathbb{E}[\mathbf{x}_t \mathbf{x}_t^H] = \mathbf{W}_t \mathbf{W}_t^H = \mathbf{W}_{s,t} \mathbf{W}_{s,t}^H + \sum_{k=1}^{K} \mathbf{R}_{k,t}, \tag{4}$$

where the rank-1 matrix $\mathbf{R}_{k,t}$ is defined as $\mathbf{R}_{k,t} \triangleq \mathbf{w}_{k,t} \mathbf{w}_{k,t}^H$, and the received signal at the k-th UE at time slot t is represented as

$$y_{k,t} = \mathbf{h}_{B,k,t}^H \mathbf{x}_t + \mathbf{h}_{r,k,t}^H \mathbf{\Phi}_t \mathbf{G}_t \mathbf{x}_t + \mathbf{h}_{r,k,t}^H \mathbf{\Phi}_t \mathbf{z}_0 + \mathbf{n}_{k,t}, \tag{5}$$

where $\mathbf{h}_{B,k,t} \in \mathbb{C}^{M \times 1}$, $\mathbf{G}_t \in \mathbb{C}^{N \times M}$, and $\mathbf{h}_{r,k,t} \in \mathbb{C}^{N \times 1}$ represent the communication links from the BS to the k-th UE, between the BS and the ARIS, and from the ARIS to the k-th UE at time slot t, respectively. It is assumed that the DFRC-BS has perfect knowledge of the channel state information (CSI) for the aforementioned channels, achieved through effective channel estimation methods [22].

We consider a general urban micro-cellular (UMi) scenario, the large-scale path loss for communication links, denoted by ρ, can be modeled as follows:

$$\rho_c \text{ [dB]} = 10\varpi \log_{10}\left(\frac{d_0}{d_s}\right) + \rho + 10\gamma \log_{10}\left(\frac{f_0}{f}\right) + \pi_{\text{ABG}}, \tag{6}$$

where ϖ and ρ denote the distance and frequency dependency coefficients, respectively. ρ is a fixed offset for path loss in dB, π_{ABG} represents the log-normal shadow fading with standard deviation σ, d_s is the distance between the transmitter and receiver, f is the carrier frequency, and $d_0 = 1m$ and $f_0 = 1$ GHz are reference values [38].

Since the communication UEs are typically located on the ground with densely surrounded scatters, Rayleigh fading channel models are employed for both $\mathbf{h}_{B,k,t}$ and $\mathbf{h}_{r,k,t}$. The channel between the BS-ARIS, denoted as $\mathbf{G}_t$, follows a Rician fading model, which encompasses both the LoS component $\mathbf{G}_{t,\text{LoS}}$ and the non-LoS (NLoS) Rayleigh fading component $\mathbf{G}_{t,\text{NLoS}}$. The LoS component is modeled as $\mathbf{G}_{t,\text{LoS}} = \mathbf{a}_{RIS}(\theta_{RIS})\mathbf{a}_{BS}^H(\theta_{BS})$, where $\mathbf{a}_{RIS}(\theta_{RIS})$ and $\mathbf{a}_{BS}^H(\theta_{BS})$ are the array response vectors of the BS antennas as well as the RIS, respectively. Furthermore. the NLoS fading component is denoted as $\mathbf{G}_{t,\text{NLoS}} \sim \mathcal{CN}(\mathbf{0}, \mathbf{\Sigma}_{RIS} \otimes \mathbf{\Sigma}_{BS})$, where $\mathbf{\Sigma}_{RIS}$ and $\mathbf{\Sigma}_{BS}$ are the spatial correlation matrices at the RIS and BS, respectively.

Furthermore, the ARIS's reflection beamforming matrix is denoted as $\mathbf{\Phi}_t \in \mathbb{C}^{N \times N}$, where $\mathbf{\Phi}_t \triangleq \text{diag}\{\phi_t\}$ is reflection matrix of the ARIS, where $\phi_t = [\phi_{1,t}..., \phi_{N,t}]^H$. Since ARIS's elements have the capability to both intelligently adjust the phase of incoming signals and amplify the reflected ones, the reflection coefficient of the n-th element of the ARIS is represented as $\phi_{n,t} \triangleq a_n e^{j\phi_{n,t}}$, $\forall n$. Here, the amplitude a_n can be continuously varied within the range $a_n \in (0, a_{\max}]$, where $a_{\max} \ge 1$ represents the maximum signal amplification provided by the amplifier. Furthermore, $\mathbf{z}_0 \sim \mathcal{CN}(0, \sigma_z^2 \mathbf{I}_N) \in \mathbb{C}^{N \times 1}$ represents the ARIS noise, where $\mathbf{I}_N$ is the identity matrix of size N. The vector $\mathbf{n}_{k,t} \sim \mathcal{CN}(0, \sigma_{k,t}^2)$ denotes the additive white Gaussian noise at the k-th UE. Based on (5), the SINR of the k-th UE at time slot t is determined as

$$\text{SINR}_{k,t}(\mathbf{W}_t, \phi_t) = \frac{\mathbf{h}_{k,t}^H \mathbf{R}_{k,t} \mathbf{h}_{k,t}}{\mathbf{h}_{k,t}^H (\mathbf{R} - \mathbf{R}_{k,t}) \mathbf{h}_{k,t} + \sigma^2 \mathbf{h}_{r,k,t}^H \mathbf{\Phi}_t \mathbf{\Phi}_t^H \mathbf{h}_{r,k,t} + \sigma_z^2}, \tag{7}$$

where we define the composite channel from the BS to the k-th UE as $\mathbf{h}_{k,t}^H = \mathbf{h}_{B,k,t}^H + \mathbf{h}_{r,k,t}^T \mathbf{\Phi}_t \mathbf{G}_t$. It is assumed that the array response or steering vector corresponding to the angle-of-arrival (AoA) or angle-of-departure (AoD) of interest is known in advance, and the ARIS-to-target link exhibits a LoS condition. For a NLoS BS-to-target link, the echo signal received via the BS-ARIS-target-ARIS-BS path at time slot t can be expressed as

$$\mathbf{y}_{s,t} = \mathbf{G}_t^H \mathbf{\Phi}_t [\mathbf{h}_{r,s,t} \beta \mathbf{h}_{r,s,t}^H \mathbf{\Phi}_t (\mathbf{G}_t \mathbf{x}_t + \mathbf{z}_0) + \mathbf{z}_1] + \mathbf{n}_{s,t}, \tag{8}$$

where β represents the amplitude of the target's radar cross-section (RCS), with an expected value given by $\mathbb{E}\{\beta^2\} = \zeta_t^2$. The channel between the ARIS and the target is $\mathbf{h}_{r,s,t} \in \mathbb{C}^{N \times 1}$. The response matrix associated with the target and

$$\text{SNR}_{s,t}(\mathbf{v}_t, \mathbf{W}_t, \phi_t) = \frac{\zeta_t^2 |\mathbf{v}_t^H \mathbf{B} \mathbf{W}_t|^2}{|\mathbf{v}_t^H \mathbf{C}|^2 \sigma_{z_0}^2 + |\mathbf{v}_t^H \mathbf{E}|^2 \sigma_{z_1}^2 + |\mathbf{v}_t^H|^2 \sigma_s^2},$$
$$= \frac{\zeta_t^2 \mathbf{v}_t^H \mathbf{B} \mathbf{W}_t \mathbf{W}_t^H \mathbf{B}^H \mathbf{v}_t}{\mathbf{v}_t^H (\sigma_{z_0}^2 \mathbf{C} \mathbf{C}^H + \sigma_{z_1}^2 \mathbf{E} \mathbf{E}^H + \sigma_s^2 \mathbf{I}_M) \mathbf{v}_t}. \tag{10}$$

the ARIS is expressed as $\mathbf{A} = \beta \mathbf{h}_{r,s,t} \mathbf{h}_{r,s,t}^H \in \mathbb{C}^{N \times N}$. Furthermore, $\mathbf{z}_1$ represents the dynamic noise introduced by the ARIS on the returning radar signal, which is assumed to be independent and has the same distribution as $\mathbf{z}_0$. A complex Gaussian distribution with mean 0 and covariance σ_s^2, times the identity matrix of size M is followed by the noise term $n_s \sim \mathcal{CN}(0_N, \sigma_s^2 \mathbf{I}_M) \in \mathbb{C}^{M \times 1}$. Since the DFRC-BS has complete knowledge of the transmitted signal in a co-located radar sensing setup, it identifies the first term in (9), which encompasses both the communication and sensing components, as the desired signal for target estimation, while treating the remaining terms as noise [21], [28]. The radar output signal at the DFRC-BS, obtained by processing the received signal $\mathbf{y}_{s,t} \in \mathbb{C}^{M \times 1}$ using the receive filter $\mathbf{v}_t \in \mathbb{C}^{M \times 1}$, at time slot t is given as

$$\mathbf{v}_t^H \mathbf{y}_{s,t} = \beta \mathbf{v}_t^H \mathbf{B} \mathbf{x}_t + \beta \mathbf{v}^H \mathbf{C} \mathbf{z}_0 + \mathbf{v}_t^H \mathbf{E} \mathbf{z}_1 + \mathbf{v}_t^H \mathbf{n}_{s,t}. \tag{9}$$

For brevity we define the equivalent channel matrix $\mathbf{B} \triangleq \mathbf{G}_t^H \boldsymbol{\Phi}_t \mathbf{A} \boldsymbol{\Phi}_t \mathbf{G}_t$, $\mathbf{C} \triangleq \mathbf{G}_t^H \boldsymbol{\Phi}_t \mathbf{A} \boldsymbol{\Phi}_t$, and $\mathbf{E} \triangleq \mathbf{G}_t^H \boldsymbol{\Phi}_t$. Thus, the target SNR at time slot t is formulated as (10) and is displayed at the top of this page.

III. PROBLEM FORMULATION

The objective is to maximize the sum of minimum SINRs of UEs within the whole ISAC period in an ARIS-assisted ISAC system while satisfying the communication and sensing quality of service (QoS) requirements. This is achieved by jointly optimizing the receive filter $\mathbf{v}_t$, transmit beamforming $\mathbf{W}_t$, ARIS reflection coefficient ϕ_t, and the trajectory of the UAV $\mathbf{q}_t$. Accordingly, the optimization problem is formulated as

$$\max_{\mathbf{v}_t, \mathbf{W}_t, \phi_t, \mathbf{q}_t, \forall t} \quad \sum_{t=1}^{T} \min_{k=1,\ldots,K} \text{SINR}_{k,t}(\mathbf{W}_t, \phi_t) \tag{11a}$$

$$\text{s.t.} \quad \text{Tr}(\mathbf{R}(\mathbf{W}_t)) \leq P_{\text{BS}}, \forall t \tag{11b}$$

$$\mathcal{P}(\mathbf{W}_t, \phi_t) \leq P_{\text{RIS}}, \forall t \tag{11c}$$

$$\text{SINR}_{k,t}(\mathbf{W}_t, \phi_t) \geq \Gamma_k, \quad \forall k \in \mathcal{K}, \tag{11d}$$

$$\text{SNR}_{s,t}(\mathbf{v}_t, \mathbf{W}_t, \phi_t) \geq \Gamma_s, \tag{11e}$$

$$\mathbf{q}_t \in \mathcal{X} \times \mathcal{Y}, \forall t \tag{11f}$$

$$a_n \leq a_{\max}, \quad \forall n \in \mathcal{N}, \tag{11g}$$

$$\sum_{t=1}^{T} \mathcal{E}_t^{\text{ARIS}}(\mathbf{q}) \leq \mathcal{E}^{\max}, \tag{11h}$$

$$\frac{\|\mathbf{q}_t - \mathbf{q}_{t-1}\|}{\eta} \leq v_{max}, \forall t, \tag{11i}$$

where

$$\mathcal{P}(\mathbf{W}_t, \phi_t) = \|\boldsymbol{\Phi}_t \mathbf{G}_t \mathbf{W}_t\|_F^2 + \|\boldsymbol{\Phi}_t \mathbf{A} \boldsymbol{\Phi}_t \mathbf{G}_t \mathbf{W}_t\|_F^2$$
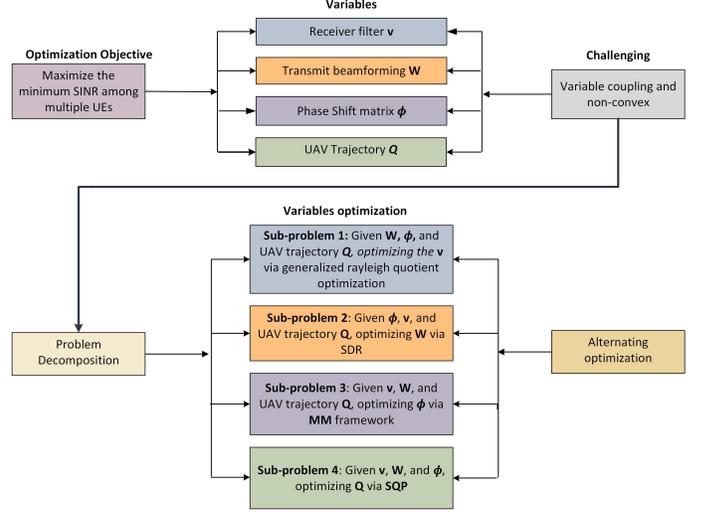

Fig. 2. Design framework of the proposed alternating optimization approach for ARIS-aided ISAC system.

$$+ \sigma_z^2 \|\boldsymbol{\Phi}_t \mathbf{A} \boldsymbol{\Phi}_t\|_F^2 + 2\sigma_z^2 \|\boldsymbol{\Phi}_t\|_F^2. \tag{12}$$

The constraints (11b) and (11c) define the power limits at the BS and the ARIS, with P_{BS} and P_{RIS} representing their respective maximum allowable power consumption. The constraints (11d) and (11e) guarantee the QoS for both the UEs and the target by ensuring that their SINR and SNR meet or exceed the predefined thresholds, Γ_k for each UE and Γ_s for the target, respectively. The constraint (11f) restricts the horizontal position of the active RIS-equipped UAV to a designated valid area. Next, the constraint (11g) ensures that the amplification factor for each ARIS element does not exceed the maximum limit, $a_{\max}$. Finally, constraints (11h) and (11i) represent the ARIS energy limitation and the maximum allowable flying speeds, respectively. The problem (11) is evidently non-convex and complicated to handle due to the non-convex objective function and the constraints (11c), (11d), (11e), and (11h).

IV. PROPOSED SOLUTION

This section introduces an alternating optimization to tackle the intricate problem (11), as illustrated in Fig. 2. The problem is divided into four subproblems, with each optimization process is updated iteratively using advanced techniques, including generalized Rayleigh quotient optimization, SDR, the MM framework, and SQP. At iteration ϱ, let $(\mathbf{v}_t^{(\varrho)}, \mathbf{W}_t^{(\varrho)}, \phi_t^{(\varrho)}, \mathbf{q}_t^{(\varrho)})$ represent the feasible point for problem (11) obtained from the $(\varrho - 1)$-th round. Firstly, problem (11) is solved to obtain the optimal solution $(\mathbf{v}_t^\star)$ for given $(\mathbf{W}_t^{(\varrho)}, \phi_t^{(\varrho)}, \mathbf{q}_t^{(\varrho)})$. Secondly, we update $\mathbf{v}_t^{(\varrho+1)} := \mathbf{v}_t^\star$ and

solve (11) to achieve the optimal solution $\mathbf{W}_t^\star$ for given $(\mathbf{v}_t^{(\varrho+1)}, \mathbf{W}_t^{(\varrho)}, \phi_t^{(\varrho)}, \mathbf{q}_t^{(\varrho)})$. Thirdly, we update $\mathbf{W}_t^{(\varrho+1)} := \mathbf{W}_t^\star$ and solve (11) to derive the optimal solution $\phi_t^\star$ for given $(\mathbf{v}_t^{(\varrho+1)}, \mathbf{W}_t^{(\varrho+1)}, \phi_t^{(\varrho)}, \mathbf{q}_t^{(\varrho)})$. Finally, we update $\phi_t^{(\varrho+1)} := \phi_t^\star$ and solve (11) to get the optimal solution $\mathbf{q}_t^\star$ for given $(\mathbf{v}_t^{(\varrho+1)}, \mathbf{W}_t^{(\varrho+1)}, \phi_t^{(\varrho+1)}, \mathbf{q}_t^{(\varrho)})$.

A. Receive Filter Optimization

For given $(\mathbf{W}_t^{(\varrho)}, \phi_t^{(\varrho)}, \mathbf{q}_t^{(\varrho)})$ and from the problem (11), it is clear that only constraint (11e) involves $\mathbf{v}_t$. As a result, the optimization of $\mathbf{v}_t$ at iteration $\varrho + 1$ can be reformulated as a problem of maximizing the $\text{SNR}_{s,t}(\mathbf{v}_t, \mathbf{W}_t, \phi_t)$, given as

$$\max_{\mathbf{v}_t} \frac{\zeta_t^2 \mathbf{v}_t^H \mathbf{F} \mathbf{v}_t}{\mathbf{v}_t^H \mathbf{\Xi} \mathbf{v}_t}, \tag{13}$$

where $\mathbf{F} = \mathbf{B}\mathbf{W}_t^{(\varrho)}(\mathbf{W}_t^{(\varrho)})^H \mathbf{B}^H \in \mathbb{C}^{M \times M}$ and $\mathbf{\Xi} = \zeta_t^2 \sigma_{z_0}^2 \mathbf{C}\mathbf{C}^H + \sigma_{z_1}^2 \mathbf{E}\mathbf{E}^H + \sigma_s^2 \mathbf{I}_M \in \mathbb{C}^{M \times M}$. It is evident that $\mathbf{F}$ and $\mathbf{\Xi}$ are Hermitian matrices, where $\mathbf{\Xi}$ is also positive semidefinite. Therefore, problem (13) can be classified as a generalized Rayleigh quotient optimization problem, which is a well-established area in optimization research [39]. The eigenvector of $\mathbf{\Xi}^{-1}\mathbf{F}$ associated with the maximum eigenvalue represents the optimal solution.

B. Transmit Beamforming Optimization

For given $(\mathbf{v}_t^{(\varrho+1)}, \mathbf{W}_t^{(\varrho)}, \phi_t^{(\varrho)}, \mathbf{q}_t^{(\varrho)})$, problem (11) at iteration $\varrho + 1$ can be rewritten as

$$\max_{\mathbf{W}_t, \forall t} \quad \sum_{t=1}^{T} \min_{k=1,\dots,K} \text{SINR}_{k,t}(\mathbf{W}_t, \phi_t^{(\varrho)}) \tag{14a}$$

$$\text{s.t.} \quad \text{Tr}(\mathbf{R}(\mathbf{W}_t)) \leq P_{\text{BS}}, \forall t, \tag{14b}$$

$$\mathcal{P}(\mathbf{W}_t, \phi_t^{(\varrho)}) \leq P_{\text{RIS}}, \forall t, \tag{14c}$$

$$\text{SINR}_{k,t}(\mathbf{W}_t, \phi_t^{(\varrho)}) \geq \Gamma_k, \quad \forall k \in \mathcal{K}, \forall t, \tag{14d}$$

$$\text{SNR}_{s,t}(\mathbf{v}_t^{(\varrho+1)}, \mathbf{W}_t, \phi_t^{(\varrho)}) \geq \Gamma_s, \forall t, \tag{14e}$$

where

$$\mathcal{P}(\mathbf{W}_t, \phi_t^{(\varrho)}) = \|\mathbf{\Phi}_t^{(\varrho)} \mathbf{G}\mathbf{W}_t\|_F^2 + \|\mathbf{\Phi}_t^{(\varrho)} \mathbf{A}\mathbf{\Phi}_t^{(\varrho)} \mathbf{G}\mathbf{W}_t\|_F^2 + \sigma_z^2 \|\mathbf{\Phi}_t^{(\varrho)} \mathbf{A}\mathbf{\Phi}_t^{(\varrho)}\|_F^2 + 2\sigma_z^2 \|\mathbf{\Phi}_t^{(\varrho)}\|_F^2. \tag{15}$$

The challenge in addressing (14) arises from the non-concavity of the objective function (14a) and the non-convexity of the constraints (14d) and (14e). To overcome this, an auxiliary variable τ_t is introduced, allowing the problem (14) to be reformulated equivalently as

$$\max_{\mathbf{W}_t, \tau_t, \forall t} \quad \sum_{t=1}^{T} \tau_t \tag{16a}$$

$$\text{s.t.} \quad \tau_t \leq \text{SINR}_{k,t}(\mathbf{W}_t, \phi_t^{(\varrho)}), \quad \forall k \in \mathcal{K}, \forall t, \tag{16b}$$

$$\tau_t \geq \Gamma_k, \quad \forall k \in \mathcal{K}, \forall t, \tag{16c}$$

$$(14b), (14c), (14e). \tag{16d}$$

Due to the non-convex nature of constraint (14e) and (16b), the problem (16) is still non-convex. By introducing auxiliary

variables $\mu \triangleq \{\mu_{k,t}\}_{\forall k,t}$, constraint (16b) can be expressed by the following two constraints:

$$\tau_t \mu_{k,t} \leq \mathbf{h}_{k,t}^H \mathbf{R}_{k,t} \mathbf{h}_{k,t}, \tag{17a}$$

$$\mu_{k,t} \geq \mathbf{h}_{k,t}^H (\mathbf{R} - \mathbf{R}_{k,t}) \mathbf{h}_{k,t} + \sigma^2 \mathbf{h}_{r,k,t}^H \mathbf{\Phi}_t \mathbf{\Phi}_t^H \mathbf{h}_{r,k,t} + \sigma_z^2, \tag{17b}$$

, $\forall k \in \mathcal{K}, \forall t$. The left-hand side of (17a) is expressed with an upper bound as follows:

$$\tau_t \mu_{k,t} \leq \frac{\tau_t^{(\varrho)}}{2\mu_{k,t}^{(\varrho)}} \mu_{k,t}^2 + \frac{\mu_{k,t}^{(\varrho)}}{2\tau_t^{(\varrho)}} \tau_t^2, \forall k \in \mathcal{K}, \forall t, \tag{18}$$

where $\tau_t^{(\varrho)}$ and $\mu_{k,t}^{(\varrho)}$ are the obtained values at the ϱ-th iteration. Hence, (17a) can be convexified as

$$\frac{\tau_t^{(\varrho)}}{2\mu_{k,t}^{(\varrho)}} \mu_{k,t}^2 + \frac{\mu_{k,t}^{(\varrho)}}{2\tau_t^{(\varrho)}} \tau_t^2 \leq \mathbf{h}_{k,t}^H \mathbf{R}_{k,t} \mathbf{h}_{k,t}, \forall k \in \mathcal{K}, \forall t. \tag{19}$$

The left-hand side of the constraint (14e) can be convexified by applying the first-order Taylor expansion, which is shown as follows [21]:

$$\mathbf{w}_t^H \mathbf{\Pi} \mathbf{w}_t \geq \tilde{\mathbf{w}}_t^{H(\varrho)} \mathbf{\Pi} \tilde{\mathbf{w}}_t^{(\varrho)} + 2\mathbb{R}\left\{ \tilde{\mathbf{w}}_t^{H(\varrho)} \mathbf{\Pi}(\mathbf{w}_t - \tilde{\mathbf{w}}_t^{(\varrho)}) \right\}, \tag{20}$$

where $\mathbf{\Pi} \triangleq \mathbf{B}^H \mathbf{v}_t \mathbf{v}_t^H \mathbf{B}$ and the aggregated beamforming vector $\mathbf{w}_t = \text{vec}(\mathbf{W}_t)$. The approximate convex formulation of (14), corresponding to iteration $\varrho + 1$, can be expressed as

$$\max_{\mathbf{W}_t, \tau_t, \mu, \forall t} \quad \sum_{t=1}^{T} \tau_t \tag{21a}$$

$$\text{s.t.} \quad \tilde{\mathbf{w}}_t^{H(\varrho)} \mathbf{\Pi} \tilde{\mathbf{w}}_t^{(\varrho)} + 2\mathbb{R}\left\{ \tilde{\mathbf{w}}_t^{H(\varrho)} \mathbf{\Pi}(\mathbf{w}_t - \tilde{\mathbf{w}}_t^{(\varrho)}) \right\} \geq \Gamma_s, \tag{21b}$$

$$\mathbf{W}_{k,t} \succeq 0, \quad \forall k \in \mathcal{K}, \tag{21c}$$

$$\text{rank}(\mathbf{W}_{k,t}) = 1, \quad \forall k \in \mathcal{K}, \tag{21d}$$

$$(14b), (14c), (16c), (17b), (19). \tag{21e}$$

By relaxing the rank-one constraint, the problem (21) is transformed into a semidefinite programming (SDP) problem that can be effectively solved using CVX [40]. Since the objective function of the original problem is upper bound, iteratively solving the reformulated problem in (21) and updating the auxiliary variables τ_t and $\mu_{k,t}$ lead to a non-decreasing sequence that converges to a local optimum. Nonetheless, the beamforming matrix $\mathbf{W}_{k,t}^*$ derived from the SDR approach may not always be rank-one. To assess the effectiveness of SDR in this context, we introduce the following theorem, which provides insights into the conditions under which the relaxation is tight.

Theorem 1: The optimal solution to problem (21), denoted as $\{\mathbf{W}_{k,t}^*, \mu_{k,t}^*, \tau_t^*\}$, is always achievable, and the matrix $\mathbf{W}_{k,t}^*$ satisfies the condition $\text{rank}(\mathbf{W}_{k,t}^*) = 1$ for each $k \in \mathcal{K}$.

Proof: Refer to Appendix A.

Theorem 1 asserts that the optimal rank-one matrix $\mathbf{W}_{k,t}^*$ can always be computed for the given problem (21). Furthermore, the optimal active beamforming vector $\mathbf{w}_{k,t}^*$ can be derived by applying the Cholesky decomposition to $\mathbf{W}_{k,t}^*$.

C. ARIS Optimization

For given $(\mathbf{v}_t^{(\varrho+1)}, \mathbf{W}_t^{(\varrho+1)}, \phi_t^{(\varrho)}, \mathbf{q}_t^{(\varrho)})$, problem (11) at iteration $\varrho + 1$ can be reformulated as

$$\max_{\phi_t, \forall t} \quad \sum_{t=1}^{T} \min_{k=1,\ldots,K} \mathrm{SINR}_{k,t}(\mathbf{v}_t^{(\varrho+1)}, \phi_t) \tag{22a}$$

$$\text{s.t.} \quad \mathcal{P}(\mathbf{W}_t^{(\varrho+1)}, \phi_t) \le P_{\mathrm{RIS}}, \forall t, \tag{22b}$$

$$\mathrm{SINR}_{k,t}(\mathbf{W}_t^{(\varrho+1)}, \phi_t) \ge \Gamma_k, \quad \forall k \in \mathcal{K}, \forall t, \tag{22c}$$

$$\mathrm{SNR}_{s,t}(\mathbf{v}_t^{(\varrho+1)}, \mathbf{W}_t^{(\varrho+1)}, \phi_t) \ge \Gamma_s, \forall t, \tag{22d}$$

$$a_n \le a_{\max}, \quad \forall n \in \mathcal{N}, \tag{22e}$$

where

$$\mathcal{P}(\mathbf{W}_t^{(\varrho+1)}, \phi_t) = \|\boldsymbol{\Phi}_t \mathbf{G}_t \mathbf{W}_t^{(\varrho+1)}\|_F^2 + \|\boldsymbol{\Phi}_t \mathbf{A} \boldsymbol{\Phi}_t \mathbf{G}_t \mathbf{W}_t^{(\varrho+1)}\|_F^2$$
$$+ \sigma_z^2 \|\boldsymbol{\Phi}_t \mathbf{A} \boldsymbol{\Phi}_t\|_F^2 + 2\sigma_z^2 \|\boldsymbol{\Phi}_t\|_F^2. \tag{23}$$

The objective function in (22a) is non-concave, while the constraints (22b)-(22d) are non-convex. To address this, the auxiliary variable χ_t is introduced, allowing the problem (22) to be equivalently rewritten as

$$\max_{\phi_t, \chi_t, \forall t} \quad \sum_{t=1}^{T} \chi_t \tag{24a}$$

$$\text{s.t.} \quad \chi_t \le \mathrm{SINR}_{k,t}(\mathbf{W}_t^{(\varrho+1)}, \phi_t), \quad \forall k \in \mathcal{K}, \forall t, \tag{24b}$$

$$\chi_t \ge \Gamma_k, \quad \forall k \in \mathcal{K}, \forall t, \tag{24c}$$

$$(22b), (22d), (22e). \tag{24d}$$

The problem in (24) is classified as non-convex due to the non-convex nature of the constraints (22b), (22d), and (24b). To handle this, we apply SDR to simplify the high-order optimization problem into a quadratic optimization framework [22]. Define $\mathbf{o} = \left[\phi_{1,t}, \ldots, \phi_{N,t}\right]^H$ as the vector containing the diagonal elements of $\boldsymbol{\Phi}_t$. By introducing an auxiliary variable φ such that $\varphi^2 = 1$, we construct the augmented vector $[\bar{\mathbf{o}} = \left[\mathbf{o}^H \quad \varphi^*\right]^H]$ and its corresponding covariance matrix $[\mathbf{O} = \bar{\mathbf{o}}\bar{\mathbf{o}}^H]$. Subsequently, the objective function and constraints in (24) are reformulated into linear and quadratic forms of $\mathbf{O}$, and the problem is solved using the SDR technique [22]. Let the equivalent channel between the BS and the k-th UE be defined as $\mathbf{H}_{k,t} = \left[\mathbf{G}_t^H \mathrm{Diag}(\mathbf{h}_{r,k,t}), \mathbf{h}_{B,k,t}\right]^H$. Accordingly, $\mathbf{h}_k^H$ is expressed as $\bar{\mathbf{o}}^H \mathbf{H}_{k,t}$. Furthermore, the remaining term $\mathbf{d}_{k,t}$ is represented as $\mathbf{h}_{r,k,t}^H \mathrm{Tr}(\hat{\mathbf{O}})\mathbf{h}_{r,k,t}\sigma^2 + \sigma_z^2$. As a result, the constraint (24b) is reformulated as

$$\mathrm{Tr}(\mathbf{R}_1 \mathbf{O}) - \chi_t(\mathrm{Tr}(\mathbf{R}_2 \mathbf{O}) + \sigma^2 \mathrm{Tr}(\hat{\mathbf{O}}\mathbf{h}_{r,k,t}\mathbf{h}_{r,k,t}^H) + \sigma_z^2) >= 0, \tag{25}$$

$\forall k \in \mathcal{K}, \forall t$, where the matrices $\mathbf{R}_1$ and $\mathbf{R}_2$ are given by $\mathbf{R}_1 \triangleq \mathbf{H}_{k,t}\mathbf{R}\mathbf{H}_{k,t}^H$ and $\mathbf{R}_2 \triangleq \mathbf{H}_{k,t}(\mathbf{R} - \mathbf{R}_{k,t})\mathbf{H}_{k,t}^H$, respectively.

Next, we then reformulate the constraint (22b) into a quadratic function of $\mathbf{O}$. The first term in (23) can be articulated as

$$\mathrm{Tr}(\boldsymbol{\Phi}_t \mathbf{A} \boldsymbol{\Phi}_t \mathbf{G}_t \mathbf{R} \mathbf{G}_t^H \boldsymbol{\Phi}_t \mathbf{H}_{k,t}^H \mathbf{A} \mathbf{H}_{k,t} \boldsymbol{\Phi}_t) \triangleq \|\mathbf{M}_1 \hat{\mathbf{o}}\|_2^2, \tag{26}$$

where $\mathbf{M}_1 = \mathbf{L}_2 \mathrm{Diag}(\mathrm{vec}(\mathbf{A}^H))$, and the positive semi-definite matrix $\mathbf{I}_N \otimes (\mathbf{G}_t \mathbf{R} \mathbf{G}_t^H) = \mathbf{L}_2 \mathbf{L}_2^H$. The second term in (23) can be represented as

$$\sigma^2 \mathrm{Tr}(\boldsymbol{\Phi}_t^H \mathbf{A} \boldsymbol{\Phi}_t \mathbf{H}_{k,t}^H \mathbf{A} \mathbf{H}_{k,t} \boldsymbol{\Phi}_t) \triangleq \|\mathbf{M}_2 \hat{\mathbf{o}}\|_2^2, \tag{27}$$

where $\mathbf{M}_2 = \sigma \mathrm{Diag}(\mathrm{vec}(\mathbf{A}^H))$. The third and fourth terms of (23) can be given by

$$\mathrm{Tr}(\boldsymbol{\Phi}_t \mathbf{G}_t \mathbf{R} \mathbf{G}_t^H \boldsymbol{\Phi}_t) = \mathrm{Tr}(\mathbf{G}_t \mathbf{R} \mathbf{G}_t^H \mathbf{O}), \tag{28}$$

and

$$\mathrm{Tr}(\boldsymbol{\Phi}_t^H \boldsymbol{\Phi}_t) = \mathrm{Tr}(\mathbf{O}). \tag{29}$$

Therefore, constraint (22b) can be reformulated as

$$\|\mathbf{M}_1 \hat{\mathbf{o}}\|_2^2 + \|\mathbf{M}_2 \hat{\mathbf{o}}\|_2^2 + \mathrm{Tr}(\mathbf{G}_t \mathbf{R} \mathbf{G}_t^H \hat{\mathbf{O}}) + 2\sigma^2 \mathrm{Tr}(\hat{\mathbf{O}}) - P_{\mathrm{RIS}} \le 0. \tag{30}$$

The left-hand side of the constraint (22d) can be convexified as [22]

$$\mathrm{Tr}\left(\mathbf{v}_t \mathbf{B} \mathbf{W}_t \mathbf{W}_t^H \mathbf{B}^H \mathbf{v}_t^H \boldsymbol{\Lambda}^{-1}\right) \ge 2\Re\left(\mathrm{Tr}\left(\mathbf{v}_t \mathbf{B} \mathbf{W}_t \mathbf{W}_t^H \mathbf{B}_i^H \mathbf{v}_t^H \boldsymbol{\Lambda}_i^{-1}\right)\right)$$
$$- \mathrm{Tr}\left(\boldsymbol{\Lambda}_i^{-1} \mathbf{v}_t \mathbf{B}_i \mathbf{W}_t \mathbf{W}_t^H \mathbf{B}_i^H \mathbf{v}_t^H \boldsymbol{\Lambda}_i^{-1} \boldsymbol{\Lambda}\right), \tag{31}$$

where $\boldsymbol{\Lambda} = \mathbf{v}^H(\sigma_{z_0}^2 \mathbf{C}\mathbf{C}^H + \sigma_{z_1}^2 \mathbf{E}\mathbf{E}^H + \sigma_r^2 \mathbf{I}_M)\mathbf{v}_t$. Further, the constraint (22e) on the power amplification gain of the active RIS can be expressed as [22]

$$[\mathrm{diag}(\bar{\mathbf{O}})]_n \le a_{\max}, \tag{32}$$

where this provides an equivalent formulation of $|a_n|^2 \le a_{\max}, \forall n \in \mathcal{N}$. To summarize, the approximate convex program for (24), solved at iteration $\varrho + 1$, is expressed as

$$\max_{\mathbf{O}, \chi_t, \forall t} \quad \sum_{t=1}^{T} \chi_t \tag{33a}$$

$$\text{s.t.} \quad \chi_t \ge \Gamma_k, \quad \forall k \in \mathcal{K}, \forall t, \tag{33b}$$

$$\mathrm{diag}(\bar{\mathbf{O}})]_{N+1} = 1, \tag{33c}$$

$$\mathrm{Rank}(\bar{\mathbf{O}}) = 1, \tag{33d}$$

$$2\Re\left(\mathrm{Tr}\left(\mathbf{B}\mathbf{W}_t \mathbf{W}_t^H \mathbf{B}_i^H \boldsymbol{\Lambda}_i^{-1}\right)\right) \tag{33e}$$

$$- \mathrm{Tr}\left(\boldsymbol{\Lambda}_i^{-1} \mathbf{B}_i \mathbf{W}_t \mathbf{W}_t^H \mathbf{B}_i^H \boldsymbol{\Lambda}_i^{-1} \boldsymbol{\Lambda}\right) \ge \Gamma_s, \forall t,$$

$$(25), (30), (32). \tag{33f}$$

The problem (33) can be transformed into an SDP problem by relaxing the constraint (33d). After obtaining $\bar{\mathbf{O}}$ by using CVX, a rank-one solution is constructed using either the Gaussian randomization method or the eigenvalue decomposition approach.

D. UAV's Trajectory Optimization

For given $(\mathbf{v}_t^{(\varrho+1)}, \mathbf{W}_t^{(\varrho+1)}, \phi_t^{(\varrho+1)}, \mathbf{q}_t^{(\varrho)})$, problem (11) at iteration $\varrho + 1$ can be rewritten as

$$\max_{\mathbf{q}_t, \forall t} f(\mathbf{q}_t) = \sum_{t=1}^{T} \min_{k=1,\ldots,K} \mathrm{SINR}_{k,t}(\mathbf{W}_t^{(\varrho+1)}, \phi_t^{(\varrho+1)}) \tag{34a}$$

$$\text{s.t.} \quad \mathrm{SINR}_{k,t}(\mathbf{W}_t^{(\varrho+1)}, \phi_t^{(\varrho+1)}) \ge \Gamma_k, \quad \forall k \in \mathcal{K}, \forall t, \tag{34b}$$

$$\mathrm{SNR}_{s,t}(\mathbf{v}_t^{(\varrho+1)}, \mathbf{W}_t^{(\varrho+1)}, \phi_t^{(\varrho+1)}) \ge \Gamma_s, \forall t, \tag{34c}$$

$$(11f), (11h), (11i). \tag{34d}$$

We utilize the SQP algorithm, which is an effective iterative method for tackling nonlinearly constrained optimization problems. Due to the presence of numerous nonlinear constraints,

the SQP approach is a good fit for the problem (34) that breaks it down into a series of quadratic subproblems, in which, each optimizing a quadratic approximation of the lagrangian function subject to linearized constraints. The UAV's position in each time slot during the ϱ-th iteration is represented as $\mathbf{q}_{t,\varrho}$. The lagrangian function $\mathcal{L}(\mathbf{q}_t)$ of the problem (34) is expressed as follows:

$$\mathcal{L}(\mathbf{q}_t, \lambda) = f(\mathbf{q}_t) + \sum_{i=1}^{K+1} \lambda_i g_i(\mathbf{q}_t), \tag{35}$$

where $f(\mathbf{q}_t)$ is the objective function, $g_i(\mathbf{q}_t)$ are simplified version of the inequality constraints of the optimization problem, such as (11h), (11i), (34b), (34c) and $\lambda = [\lambda_1, \lambda_2, ...\lambda_{K+1}]$ represent the dual Lagrange multipliers corresponding to the constraints.

The SQP method converges in a finite number of iterations for solving (34). At each iteration ϱ, it transforms the optimization problem into a QP subproblem:

$$\min_{\Delta \mathbf{q}_t} \quad \frac{1}{2}\Delta(\mathbf{q}_t)^T \mathbf{D}_{k,t} \Delta \mathbf{q}_t + \nabla f(\mathbf{q}_t)^T \Delta \mathbf{q}_t$$
$$\text{s.t.} \quad g_{i,t}\mathbf{q}_{t,\varrho} + \nabla g_{i,t}(\mathbf{q}_{t,\varrho})^T \Delta \mathbf{q}_t \leq 0, \quad \forall i, \tag{36}$$

where $\mathbf{D}_{k,t}$ is the Hessian matrix of the lagrangian, and $\nabla f(\mathbf{q}_t)$ and $\nabla g_{i,t}(\mathbf{q}_{t,\varrho})$ are the gradients of the objective function and the constraints, respectively.

The SQP approach updates the pair of solutions $(\mathbf{q}_{t,\varrho}, \lambda_\varrho)$ to optimize the function $\mathcal{L}$. Specifically, the dual Lagrange variables, the UAV's 2-D location and trajectory variable are refined by computing the correction vector $\mathbf{s}_\varrho = \begin{bmatrix} \varsigma_{q,\varrho}^T & \varsigma_{\lambda,\varrho}^T \end{bmatrix}^T$ at the ϱ-th iteration. The update process is expressed as follows:

$$\mathbf{q}_{t,(\varrho+1)} = \mathbf{q}_{t,\varrho} + \beta_{q_t,\varrho} \varsigma_{\mathbf{q},\varrho}, \tag{37}$$

$$\lambda_{(\varrho+1)} = \lambda_\varrho + \beta_{\lambda,\varrho} \varsigma_{\lambda,\varrho}, \tag{38}$$

where $\beta_{\mathbf{q}_t,\varrho}$ and $\beta_{\lambda,\varrho}$ are non-negative step sizes determined by line search methods to ensure convergence. The correction vector $\Delta \mathbf{q}_{t,\varrho}$ is determined by solving the QP problem given below

$$\begin{bmatrix} \nabla_{\mathbf{q}_t}^2 \mathcal{L}(\mathbf{q}_{t,\varrho}, \lambda_\varrho) & \nabla g(\mathbf{q}_t)^T \\ \nabla g(\mathbf{q}_t) & 0 \end{bmatrix} \begin{bmatrix} \varsigma_{\mathbf{q},\varrho,t} \\ -\varsigma_{\lambda,\varrho,t} \end{bmatrix} = - \begin{bmatrix} \nabla_{\mathbf{q}_t} \mathcal{L}(\mathbf{q}_{t,\varrho}, \lambda_\varrho) \\ g(\mathbf{q}_\varrho) \end{bmatrix}$$

, where the first-order and second-order partial derivatives are represented by $\nabla[\mathcal{L}(\mathbf{q}_{t,\varrho}, \lambda_\varrho)]$ and $\nabla^2[\mathcal{L}(\mathbf{q}_{t,\varrho}, \lambda_\varrho)]$, respectively, where the Hessian matrix is denoted as $\nabla^2[\cdot]$.

Furthermore, in (35), the KKT conditions are employed to solve the SQP quadratic problem. In particular, the condition $\nabla[\mathbf{q}_{t,i}(\mathbf{q}_t)]\varsigma + \mathbf{q}_{t,i}(\mathbf{q}_t) = 0$ is employed to ensure that the constraints remain active during each iteration. SQP progressively refines the solution estimate with each iteration, converging to the optimal solution in a finite number of iteration. The step size parameters $\beta_{\mathbf{q}_t,\varrho}$ and $\beta_{\lambda,\varrho}$ are determined using a merit function, ensuring the step size reduces the function's value. This approach can be implemented using standard optimization tools like MATLAB's CVX toolbox.

Finally, the optimal 2-D positioning of the UAV within the coordinated framework can be determined by adhering to the described steps. The proposed alternating algorithm for solving problem (11) is outlined in Algorithm 1.

Algorithm 1 Proposed Iterative Alternating Optimization Algorithm for Solving Problem (11)

Initialization: Initialize $\varrho := 0$ and generate an initial feasible solution $(\mathbf{v}_t^{(0)}, \mathbf{W}_t^{(0)}, \phi_t^{(0)}, \mathbf{q}_t^{(0)}), \forall t$.

1: **repeat**
2:     With $(\mathbf{W}_t^{(\varrho)}, \phi_t^{(\varrho)}, \mathbf{q}_t^{(\varrho)})$, solve problem (13) to compute the optimal $\mathbf{v}_t^\star$, and update $\mathbf{v}_t^{(\varrho+1)} := \mathbf{v}_t^\star$;
3:     With $(\mathbf{v}_t^{(\varrho+1)}, \mathbf{W}_t^{(\varrho)}, \phi_t^{(\varrho)}, \mathbf{q}_t^{(\varrho)})$, solve the reformulated problem (21) to determine $\mathbf{W}_t^\star$, and update $\mathbf{W}_t^{(\varrho+1)} := \mathbf{W}_t^\star$;
4:     With $(\mathbf{v}_t^{(\varrho+1)}, \mathbf{W}_t^{(\varrho+1)}, \phi_t^{(\varrho)}, \mathbf{q}_t^{(\varrho)})$, solve problem (33) to find the optimal $\phi_t^\star$, and update $\phi_t^{(\varrho+1)} := \phi_t^\star$;
5:     With $(\mathbf{v}_t^{(\varrho+1)}, \mathbf{W}_t^{(\varrho+1)}, \phi_t^{(\varrho+1)}, \mathbf{q}_t^{(\varrho)})$, solve problem (36) to calculate $\mathbf{q}_t^\star$, and update $\mathbf{q}_t^{(\varrho+1)} := \mathbf{q}_t^\star$;
6:     Fix $\varrho := \varrho + 1$;
7: **until** Convergence criterion is satisfied.
8: **Output**: $(\mathbf{v}_t^{(\varrho)}, \mathbf{W}_t^{(\varrho)}, \phi_t^{(\varrho)}, \mathbf{q}_t^{(\varrho)})$.

Convergence Analysis: Due to the iterative nature of Algorithm 1, it is crucial to analyze its convergence to validate its effectiveness. Let $(\mathbf{v}_t^{(\varrho)}, \mathbf{W}_t^{(\varrho)}, \phi_t^{(\varrho)}, \mathbf{q}_t^{(\varrho)})$ represent the feasible solutions at the ϱ-th iteration. The iterative optimization process progresses as $\cdots \rightarrow (\mathbf{v}_t^{(\varrho)}, \mathbf{W}_t^{(\varrho)}, \phi_t^{(\varrho)}, \mathbf{q}_t^{(\varrho)}) \rightarrow (\mathbf{v}_t^{(\varrho+1)}, \mathbf{W}_t^{(\varrho)}, \phi_t^{(\varrho)}, \mathbf{q}_t^{(\varrho)}) \rightarrow (\mathbf{v}_t^{(\varrho+1)}, \mathbf{W}_t^{(\varrho+1)}, \phi_t^{(\varrho)}, \mathbf{q}_t^{(\varrho)}) \rightarrow (\mathbf{v}_t^{(\varrho+1)}, \mathbf{W}_t^{(\varrho+1)}, \phi_t^{(\varrho+1)}, \mathbf{q}_t^{(\varrho)}) \rightarrow (\mathbf{v}_t^{(\varrho+1)}, \mathbf{W}_t^{(\varrho+1)}, \phi_t^{(\varrho+1)}, \mathbf{q}_t^{(\varrho+1)}) \rightarrow \ldots$. For problem (13) which involves solving the Rayleigh quotient optimization, the process is constrained by the largest eigenvalue. As a result, solving this problem leads to a non-decreasing trend in the minimum SINR, expressed as

$$\text{SINR}^{(\varrho+1)}(\mathbf{v}_t^{(\varrho+1)}, \mathbf{W}_t^{(\varrho)}, \phi_t^{(\varrho)}, \mathbf{q}_t^{(\varrho)})$$
$$\geq \text{SINR}^{(\varrho)}(\mathbf{v}_t^{(\varrho)}, \mathbf{W}_t^{(\varrho)}, \phi_t^{(\varrho)}, \mathbf{q}_t^{(\varrho)}). \tag{39}$$

Similarly, for problem (21) which is convex in $\mathbf{W}_t$ and solved as a maximization problem, the SINR continues to improve, ensuring:

$$\text{SINR}^{(\varrho+1)}(\mathbf{v}_t^{(\varrho+1)}, \mathbf{W}_t^{(\varrho+1)}, \phi_t^{(\varrho)}, \mathbf{q}_t^{(\varrho)})$$
$$\geq \text{SINR}^{(\varrho+1)}(\mathbf{v}_t^{(\varrho+1)}, \mathbf{W}_t^{(\varrho)}, \phi_t^{(\varrho)}, \mathbf{q}_t^{(\varrho)}). \tag{40}$$

On the other hand, $\phi_t^{(\varrho+1)}$ is derived as the solution to problem (33), the minimum SINR further satisfies:

$$\text{SINR}^{(\varrho+1)}(\mathbf{v}_t^{(\varrho+1)}, \mathbf{W}_t^{(\varrho+1)}, \phi_t^{(\varrho+1)}, \mathbf{q}_t^{(\varrho)})$$
$$\geq \text{SINR}^{(\varrho+1)}(\mathbf{v}_t^{(\varrho+1)}, \mathbf{W}_t^{(\varrho+1)}, \phi_t^{(\varrho)}, \mathbf{q}_t^{(\varrho)}). \tag{41}$$

Finally, $\mathbf{q}_t^{(\varrho+1)}$ represents the optimal solution to the problem (36), and it can be expressed as

$$\text{SINR}^{(\varrho+1)}(\mathbf{v}_t^{(\varrho+1)}, \mathbf{W}_t^{(\varrho+1)}, \phi_t^{(\varrho+1)}, \mathbf{q}_t^{(\varrho+1)})$$
$$\geq \text{SINR}^{(\varrho+1)}(\mathbf{v}_t^{(\varrho+1)}, \mathbf{W}_t^{(\varrho+1)}, \phi_t^{(\varrho+1)}, \mathbf{q}_t^{(\varrho)}). \tag{42}$$

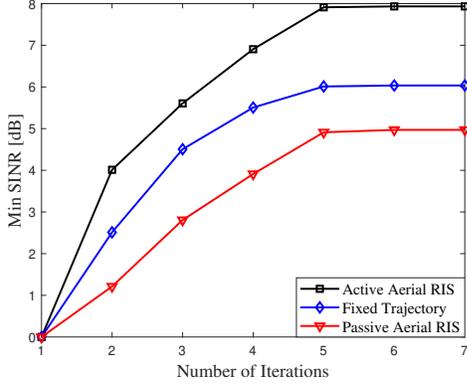Thus, the minimum SINR, which serves as the objective function, exhibits a monotonic, non-decreasing behavior at

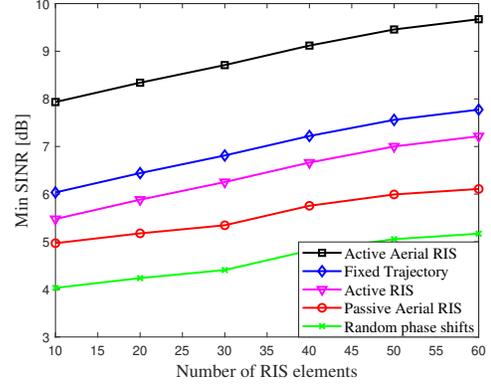Fig. 3. Convergence behavior of Algorithm 1.

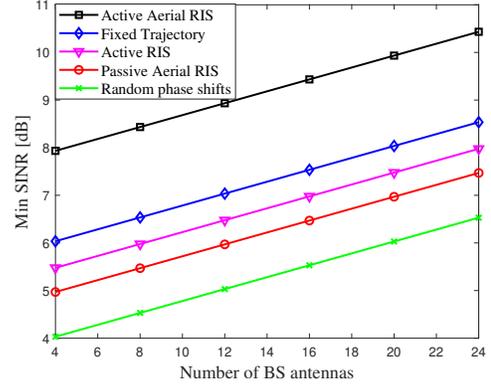Fig. 4. The effect of number of RIS elements on the minimum SINR of UEs.

Fig. 5. The effect of BS antenna count on the minimum SINR of UEs.

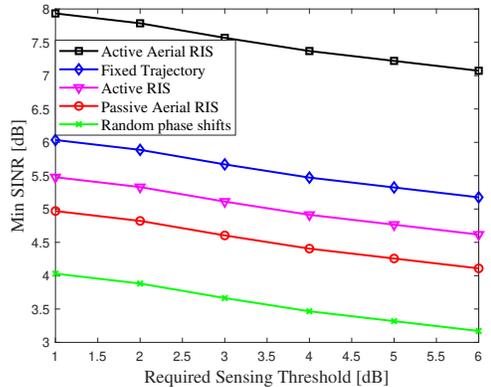Fig. 6. The impact of sensing threshold requirements on the minimum SINR of UEs.

every iteration. Since the SINR, being inherently constrained by the power budget and path loss, ensures that the algorithm converges to a stable and well-defined solution. Although the Gaussian randomization or maximum eigenvalue approximation for rank-one constraints may introduce some performance degradation, the AO method guarantees convergence to a locally optimal solution that satisfies the KKT conditions.

Complexity Analysis: The computational complexity of the proposed algorithm plays a significant role. In each iteration, the complexities associated with optimizing $\mathbf{v}_t$, $\mathbf{W}_t$, ϕ_t, and $\mathbf{q}_t$ are outlined as follows:

- Optimization of $\mathbf{v}_t$: This step involves eigenvalue decomposition and the computation of optimal solutions to maximize the minimum SINR. The complexity is approximately $\mathcal{O}(M^3)$ [39].
- Optimization of $\mathbf{W}_t$: Solving problem (21) involves SDP and eigenvalue decomposition to extract a rank-one solution. By applying the interior point algorithm, the complexity of solving the SDP problem (21) without the rank-one constraint is $O(M^{4.5} \log(\epsilon^{-1}))$, where ϵ denotes the accuracy tolerance [41]. The complexity of the eigenvalue decomposition required to recover the rank-one result is $O(KM^3)$ [39].
- Optimization of ϕ_t: Optimizing ϕ_t entails solving the SDP problem (33) and performing a rank-one decomposition. The complexity of solving (33), after relaxing the rank-one constraint, is $O(N^{4.5} \log(\epsilon^{-1}))$, while the eigenvalue decomposition to recover the rank-one solution requires $O(N^3)$ [39].
- Optimization of $\mathbf{q}_t$: The complexity of solving the SQP problem (36) is $O(\log(\log(\epsilon^{-1}))2^{3.5})$, where the term $O(\log(\log(\epsilon^{-1})))$ signifies the rapid convergence characteristic of the SQP method [42].

Overall, the computational complexity per iteration of Algorithm 1 is $\mathcal{O}(M^3 + M^{4.5} \log(\epsilon^{-1}) + KM^3 + N^{4.5} \log(\epsilon^{-1}) + N^3 + \log(\log(\epsilon^{-1}))2^{3.5})$.

V. NUMERICAL RESULTS

This section provides numerical results to evaluate the effectiveness of the proposed algorithm. The BS is equipped with $M = 4$ antennas, enabling communication with $K = 3$ UEs while simultaneously sensing the target. The BS and the target are positioned at coordinates (0, 0) and (-10 m, 35 m), respectively. The UEs are uniformly and randomly distributed in a circular area centered at (5 m, 30 m) with a radius of 10 m [22]. The ARIS, consisting of $N = 10$ reflection units, is initially positioned at (-50 m, 35 m). A threshold of 1 dB is set for the sensing SNR. The system operates at a carrier frequency of 2.7 GHz, and the target has a RCS of 1 m². The ARIS is assumed to have a maximum power amplification gain of 4 dB. The channel bandwidth is set to 10 MHz, while the noise power density at the BS, UEs, and ARIS is −174 dBm/Hz.

We use MATLAB 2022b and the SDPT3 solver to solve the convex program, where the iterative process of each algorithm
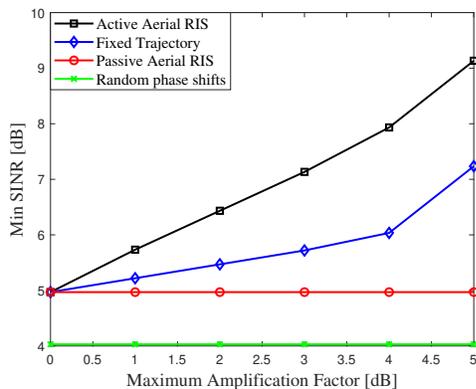
Fig. 7. The impact of maximum amplification factor on the minimum SINR of UEs.

Fig. 8. The 2D UAV's trajectory.

is terminated when the improvement in the objective function between two successive iterations falls below 10^{-3}. The proposed algorithm's performance is analyzed by benchmarking it against four reference schemes, detailed as follows:

- Fixed UAV's trajectory with ARIS: In this scheme, the ARIS optimizes its phase shifts and amplifies signals, but the UAV follows a static, fixed trajectory.
- Active RIS: This benchmark uses an active RIS which is installed in a fixed location like wall or rooftop.
- Passive aerial RIS with trajectory optimization: the UAV's trajectory is optimized to enhance SINR performance, but the RIS is passive and can only reflect signals without amplification.
- Passive aerial RIS with random phase shifts: This benchmark uses a passive RIS whose phase shifts are assigned randomly without any optimization.

To simplify the representation in simulation figures, our proposed system, the first, the second, the third, and the fourth baseline schemes are labeled as "Active Aerial RIS", "Fixed Trajectory", "Active RIS", "Passive Aerial RIS", and "Random phase shifts", respectively.

Fig. 3 illustrates the convergence behavior of Algorithm 1 in terms of minimum SINR. The algorithm converges to the optimal value within approximately five iterations on average across all cases, demonstrating its effectiveness.

Figure 4 illustrates the relationship between the minimum SINR and the number of RIS elements. Apparently, the minimum SINR significantly improves as the number of RIS elements increases across all cases due to the higher degree of freedom and diversity gain provided by additional elements for manipulating wireless environment. Further, the effectiveness of the proposed scheme is much higher than that of the fixed trajectory scheme as the optimized UAV's trajectory ensures optimal positional placement for both communication UEs and sensing the target. Besides, the proposed scheme considerably outperforms both passive aerial RIS with trajectory optimization and random phase shifts cases, confirming the benefit of deploying active RIS. This is due to the active RIS's capability to overcome the impact of multiplicative fading. Also, the active RIS with controllable amplitude offers the advantage of channel enhancement over the passive RIS. Additionally, the active RIS, with its ability to reflect signal,
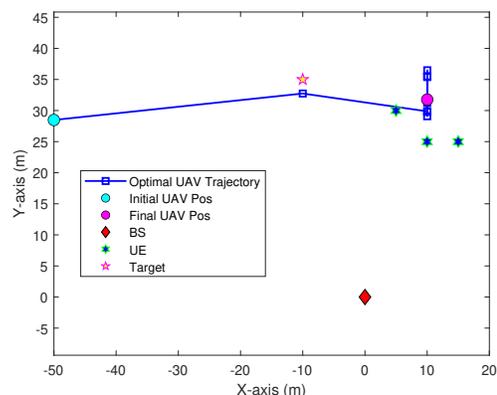
can boost the strength of the reflected signals directed towards the UEs, further improving communication performance by strengthening signal propagation.

Fig. 5 depicts the effect of BS's antennas on the minimum SINR. As expected, increasing M results in higher minimum SINR for all schemes. This is because increasing the number of antennas at the BS can provide more spatial diversity and larger beamforming gains. Also, the proposed method attains a superior minimum SINR compared to other alternative baseline schemes.

Fig. 6 illustrates the relationship between the minimum SINR of communication UEs and the required SNR sensing threshold. Interestingly, the increase in the required sensing threshold results in the degradation of minimum SINR of communication UEs for all schemes. This occurs because a higher required sensing threshold demands more power for target sensing, leaving less power for communication, which ultimately results in a decrease in the minimum SINR of communication UEs. Thus, it underscores the trade-off between sensing and communication performance.

Fig. 7 demonstrates how the maximum amplification factor influences the minimum SINR of communication UEs. Unsurprisingly, the minimum SINR of communication UEs considerably enhances with the increase in maximum amplification factor for the proposed and fixed trajectory schemes. This is due to the fact that the greater amplification capability of the active RIS significantly enhances the channel conditions, thereby improving the minimum communication SINR performance.

Fig. 8 shows the trajectory of ARIS as it moves from its initial to optimized position using the SQP algorithm. Initially, the UAV is located far from the UEs and the sensing target, but as the optimization progresses, it gradually moves closer to the UEs' region. This movement helps strengthen the reflected communication links and improves sensing performance, as the ARIS can dynamically amplify and direct signals. The UAV flies in a path that brings it to locations where it can best serve multiple UEs simultaneously while maintaining effective coverage of the sensing target, resulting in an improved overall system performance.

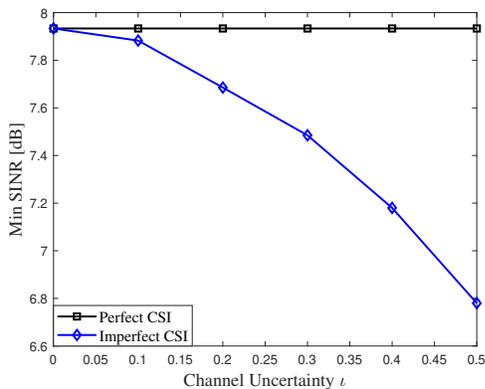Unlike passive RIS systems, where knowledge of the cas-

Fig. 9. The effect of channel uncertainty on the minimum SINR of UEs.

caded BS-RIS-UE channel is typically sufficient for optimizing transceiver parameters and RIS phase shifts, active RIS systems require access to the individual CSI of the BS-to-RIS channel $\mathbf{G}_t$ and the RIS-UE channel $\mathbf{h}_{r,k,t}$. This is because calculating critical performance metrics such as the communication SINR (7), the radar SNR (10), and the RIS transmit power (11c) relies on precise knowledge of these separate links. However, acquiring such individual CSI is particularly challenging in active RIS deployments due to their limited signal processing capabilities. To account for these practical limitations and illustrate the robustness of the proposed optimization scheme, we introduce a benchmark that incorporates estimation errors in both $\mathbf{G}_t$ and $\mathbf{h}_{r,k,t}$. A bounded CSI error model is adopted, where $\mathbf{G} = \hat{\mathbf{G}}_t + \Delta\mathbf{G}_t$, $\mathbf{h}_{r,k,t} = \hat{\mathbf{h}}_{r,k,t} + \Delta\mathbf{h}_{r,k,t}$, with $\hat{\mathbf{G}}_t$ and $\hat{\mathbf{h}}_{r,k,t}$ representing the estimated CSI at the BS. The unknown errors $\Delta\mathbf{G}_t$ and $\Delta\mathbf{h}_{r,k,t}$ are bounded by $\|\Delta\mathbf{G}_t\|_F \leq \iota\|\mathbf{G}_t\|_F$ and $\|\Delta\mathbf{h}_{r,k,t}\|_2 \leq \iota\|\mathbf{h}_{r,k,t}\|_2$, respectively, where $\iota \in [0,1)$ denotes the relative degree of CSI uncertainty. This formulation enables a more realistic performance evaluation of the proposed system under imperfect CSI conditions.

Fig. 9 illustrates how the minimum SINR varies with different levels of channel uncertainty. It is clear that the minimum SINR drops significantly with the increase in the channel uncertainty level, thus highlighting the detrimental impact of imferfect CSI on the system performance.

VI. CONCLUSION

This study focuses on improving the sum of minimum SINRs of communication UEs within the whole ISAC period in an ISAC system that incorporates a UAV equipped with an active RIS. The aim is to maximize the sum of minimum SINRs of UEs within the whole ISAC period by optimizing BS's transmit beamforming matrix and receive filter, the ARIS's reflection coefficients, and the UAV's trajectory, while ensuring compliance with power limitations, and SINR demand for UEs and the SNR target echo signal. To address the complexities of this highly non-convex problem, an efficient alternating optimization framework is proposed. This framework integrates techniques including generalized Rayleigh quotient optimization, SDR, MM framework, and SQP to solve this intricate problem. Simulation results confirm the rapid convergence of the proposed approach and demonstrate significant improvements in the minimum SINR for the

ARIS-assisted ISAC system compared to systems with fixed UAV's trajectory, active RIS, passive RIS, or random phase shifts. Our future work will focus on extending the proposed framework to more practical scenarios involving imperfect CSI, incorporating robust optimization techniques to address estimation errors and uncertainties in dynamic environments.

APPENDIX A

PROOF OF THEOREM 1

When the rank-one constraint is omitted, problem (21) becomes jointly concave with respect to the variables $\{W_{k,t}, \mu_{k,t}, \tau_t\}$ and satisfies Slater's condition [43]. Consequently, strong duality holds, and the Lagrangian function of problem (21) with respect to the variable $W_{k,t}$ can be expressed as

$$
\begin{aligned}
\mathcal{F}&\{\tau_t, \mu_{k,t}, \zeta_{k,t}, \ell_{k,t}, \alpha_{k,t}, \delta_{k,t}, \omega_{k,t}, \boldsymbol{\Omega}_{k,t}, \mathbf{W}_{k,t}\} \\
&= \zeta_{k,t}\left(P_{BS} - \mathrm{Tr}(\mathbf{R}(\mathbf{W}_{k,t}))\right) \\
&\quad + \ell_{k,t}\left(P_{RIS} - \left\|\boldsymbol{\phi}_t^{(\varrho)}\mathbf{GW}_t\right\|_F^2 - \left\|\boldsymbol{\phi}_t^{(\varrho)}\mathbf{A}\boldsymbol{\phi}_t^{(\varrho)}\mathbf{GW}_t\right\|_F^2\right) \\
&\quad + \alpha_{k,t}\left(\mathbf{w}_{k,t}^H\boldsymbol{\Pi}\mathbf{w}_{k,t}\right) + \delta_{k,t}\left(\mathbf{h}_{k,t}^H(\mathbf{R}-\mathbf{R}_{k,t})\mathbf{h}_{k,t}\right) \\
&\quad + \omega_{k,t}\left(\mathbf{h}_{k,t}^H\mathbf{R}_{k,t}\mathbf{h}_{k,t} - \frac{\tau_t^{(\varrho)}}{2\mu_{k,t}^{(\varrho)}}\mu_{k,t}^2 - \frac{\mu_{k,t}^{(\varrho)}}{2\tau_t^{(\varrho)}}\tau_t^2\right) \\
&\quad + \mathrm{Tr}(\boldsymbol{\Omega}_{k,t}\mathbf{W}_{k,t}) + \varepsilon, \quad\quad\quad (43)
\end{aligned}
$$

where the variables $\tau_t, \mu_{k,t}, \zeta_{k,t}, \ell_{k,t}, \alpha_{k,t}, \delta_{k,t}, \omega_{k,t}$, and $\boldsymbol{\Omega}_{k,t}$ denote the Lagrange multipliers corresponding to constraints (14b), (14c), (17b), (19), and (21b), respectively. Additionally, ε includes all terms that are independent of $\mathbf{W}_{k,t}$. To investigate the structure of the optimal solution $\mathbf{W}_{k,t}^*$, it is important to verify whether the Karush-Kuhn-Tucker (KKT) conditions for problem (21) are satisfied. These KKT conditions characterize the criteria for optimal beamforming, which can be given by

$$
\boldsymbol{\Omega}_{k,t}^*\mathbf{W}_{k,t}^* = 0, \quad\quad\quad (44)
$$

$$
\nabla_{\mathbf{w}_{k,t}}\mathcal{F}\left(\mathbf{W}_{k,t}^*\right) = \boldsymbol{\vartheta}_{k,t}^* - \boldsymbol{\Omega}_{k,t}^* = 0, \qu\quad (45)
$$

$$
\zeta_{k,t}^*, \ell_{k,t}^*, \alpha_{k,t}^*, \delta_{k,t}^*, \omega_{k,t}^*, \boldsymbol{\Omega}_{k,t}^* \geq 0. \qu\quad (46)
$$

The optimum Lagrangian multipliers are denoted as $\zeta_{k,t}^*, \ell_{k,t}^*, \alpha_{k,t}^*, \delta_{k,t}^*, \omega_{k,t}^*$, and $\boldsymbol{\Omega}_{k,t}^*$, while $\boldsymbol{\vartheta}_{k,t}^*$ can be represented as

$$
\boldsymbol{\vartheta}_{k,t}^* = \zeta_{k,t}^*\boldsymbol{I}_M - \boldsymbol{\xi}_{k,t}^*, \qu\quad\quad (47)
$$

where $\boldsymbol{\xi}_{k,t}^* = \ell_{k,t}^*\left(\left\|\boldsymbol{\phi}_t^{(\varrho)}\mathbf{G}\right\|_F^2 + \left\|\boldsymbol{\phi}_t^{(\varrho)}\mathbf{A}\boldsymbol{\phi}_t^{(\varrho)}\mathbf{G}\right\|_F^2\right) + \alpha_{k,t}^*\boldsymbol{\Pi} + \delta_{k,t}^*\left(\mathbf{h}_{k,t}^H\mathbf{h}_{k,t}\right) + \omega_{k,t}^*\left(\mathbf{h}_{k,t}^H\mathbf{h}_{k,t}\right)$. We assume that the largest eigenvalue of the matrix $\boldsymbol{\xi}_{k,t}^*$ is denoted by $\xi_{k,t}^* \in \mathbb{R}$. According to equation (46), if $\xi_{k,t}^* > \zeta_{k,t}^*$, then the condition $\boldsymbol{\vartheta}_{k,t}^* \geq 0$ does not hold, which contradicts the assumption that $\zeta_{k,t}^* > 0$.

However, when $\xi_{k,t}^* \leq \zeta_{k,t}^*$, the matrix $\boldsymbol{\vartheta}_{k,t}^*$ is positive semidefinite, and its rank satisfies $\text{rank}(\boldsymbol{\vartheta}_{k,t}^*) \geq M - 1$. Therefore, we can further derive that

$$\text{rank}(\boldsymbol{\Omega}_{k,t}^*) \geq M - 1. \tag{48}$$

It is evident that the matrix $\boldsymbol{\Omega}_{k,t}^*$ can have a rank of either M or $M - 1$. If the rank is M, the condition for optimal power cannot be satisfied. In this case, the corresponding beamforming matrix $\mathbf{W}_{k,t}^*$ would have zero rank, meaning that the BS would not transmit any signal. To prevent this, the rank must be $M - 1$, ensuring that $\mathbf{W}_{k,t}^*$ lies within the null space of $\boldsymbol{\Omega}_{k,t}^*$. As a result, the optimal beamforming matrix is represented by a rank-one decomposition, where $\mathbf{W}_{k,t}^*$ is the outer product of a vector $\mathbf{w}_{k,t}^*$ and its conjugate transpose. This structure confirms that $\mathbf{W}_{k,t}^*$ is the optimal solution for the beamforming problem (21).

REFERENCES

[1] X. Zhu *et al.*, "Enabling intelligent connectivity: A survey of secure ISAC in 6G networks," *IEEE Commun. Surv. Tutor.*, pp. 1–34, July 2024.

[2] C.-X. Wang *et al.*, "On the road to 6G: Visions, requirements, key technologies, and testbeds," *IEEE Commun. Surv. Tutor.*, vol. 25, no. 2, pp. 905–974, Feb. 2023.

[3] N. González-Prelcic *et al.*, "The integrated sensing and communication revolution for 6G: Vision, techniques, and applications," *Proc. IEEE*, vol. 112, no. 7, pp. 676–723, July 2024.

[4] A. Liu *et al.*, "A survey on fundamental limits of integrated sensing and communication," *IEEE Commun. Surv. Tutor.*, vol. 24, no. 2, pp. 994–1034, Feb. 2022.

[5] D. Wang *et al.*, "Uplink secrecy performance of RIS-based RF/FSO three-dimension heterogeneous network," *IEEE Trans. Wirel. Commun.*, vol. 23, no. 3, p. 1798–1809, Mar. 2024.

[6] S. Shakoor *et al.*, "Integrated sensing and communications for reconfigurable intelligent surface-aided cell-free networks," *IEEE Commun. Lett.*, pp. 1–1, Apr. 2025.

[7] Q. Wu *et al.*, "Intelligent reflecting surface-aided wireless communications: A tutorial," *IEEE Trans. Commun.*, vol. 69, no. 5, pp. 3313–3351, May 2021.

[8] L. Yashvanth and C. R. Murthy, "Performance analysis of intelligent reflecting surface assisted opportunistic communications," *IEEE Trans. Signal Process.*, vol. 71, pp. 2056–2070, Apr. 2023.

[9] Y. Zhang, C. You, and B. Zheng, "Multi-active multi-passive (MAMP)-IRS aided wireless communication: A multi-hop beam routing design," *IEEE J. Sel. Areas Commun.*, vol. 41, no. 8, pp. 2497–2513, Aug. 2023.

[10] L. Chen, X. Yuan, and Y.-J. A. Zhang, "Coverage analysis of RIS-assisted mmwave cellular networks with 3D beamforming," *IEEE Trans. Commun*, vol. 72, no. 6, pp. 3618–3633, June 2024.

[11] M. Hua *et al.*, "Secure intelligent reflecting surface-aided integrated sensing and communication," *IEEE Trans. Wirel. Commun.*, vol. 23, no. 1, pp. 575–591, Jan. 2024.

[12] H. Luo, R. Liu, M. Li, and Q. Liu, "RIS-aided integrated sensing and communication: Joint beamforming and reflection design," *IEEE Trans. Veh. Technol.*, vol. 72, no. 7, pp. 9626–9630, July 2023.

[13] K. Meng *et al.*, "UAV trajectory and beamforming optimization for integrated periodic sensing and communication," *IEEE Wirel. Commun. Lett.*, vol. 11, no. 6, pp. 1211–1215, Mar. 2022.

[14] ——, "UAV-enabled integrated sensing and communication: Opportunities and challenges," *IEEE Wirel. Commun.*, vol. 31, no. 2, pp. 97 –104, Apr. 2024.

[15] S. Shakoor *et al.*, "Role of UAVs in public safety communications: Energy efficiency perspective," *IEEE Access*, vol. 7, pp. 140 665–140 679, Sep. 2019.

[16] M. K. Banafaa *et al.*, "A comprehensive survey on 5G-and-beyond networks with UAVs: Applications, emerging technologies, regulatory aspects, research trends and challenges," *IEEE Access*, vol. 12, pp. 7786–7826, Jan. 2024.

[17] L. Li *et al.*, "Unmanned aerial vehicles towards future industrial internet: Roles and opportunities," *Digit. Commun. Netw.*, vol. 10, no. 4, pp. 873–883, Aug. 2024.

[18] Z. Zhai *et al.*, "Energy-efficient UAV-mounted RIS assisted mobile edge computing," *IEEE Wirel. Commun. Lett.*, vol. 11, no. 12, pp. 2507–2511, Dec. 2022.

[19] M. Najafi, V. Jamali, R. Schober, and H. V. Poor, "Physics-based modeling and scalable optimization of large intelligent reflecting surfaces," *IEEE Trans. Commun.*, vol. 69, no. 4, pp. 2673–2691, Apr. 2021.

[20] D. Xu *et al.*, "Optimal resource allocation design for large IRS-assisted SWIPT systems: A scalable optimization framework," *IEEE Trans. Commun.*, vol. 70, no. 2, pp. 1423–1441, Feb. 2022.

[21] Q. Zhu, M. Li, R. Liu, and Q. Liu, "Joint transceiver beamforming and reflecting design for active RIS-aided ISAC systems," *IEEE Trans. Veh. Technol.*, vol. 72, no. 7, pp. 9636–9640, July 2023.

[22] Z. Yu *et al.*, "Active RIS aided ISAC systems: Beamforming design and performance analysis," *IEEE Trans. Commun.*, vol. 72, no. 3, pp. 1578–1595, Mar. 2024.

[23] R. Liu *et al.*, "Integrated sensing and communication with reconfigurable intelligent surfaces: Opportunities, applications, and future directions," *IEEE Trans. Wirel. Commun.*, vol. 30, no. 1, pp. 50–57, Feb. 2023.

[24] X. Yang *et al.*, "RIS-assisted cooperative multicell ISAC systems: A multi-user and multi-target case," *IEEE Trans. Wirel. Commun.*, vol. 23, no. 8, pp. 8683–8699, Aug. 2024.

[25] H. Lu, Y. Zeng, S. Jin, and R. Zhang, "Aerial intelligent reflecting surface: Joint placement and passive beamforming design with 3D beam flattening," *IEEE Trans. Wirel. Commun.*, vol. 20, no. 7, pp. 4128–4143, July 2021.

[26] K. Zhong *et al.*, "Joint waveform and beamforming design for RIS-aided ISAC systems," *IEEE Signal Process. Lett.*, vol. 30, pp. 165–169, Feb. 2023.

[27] D. An, J. Hu, and C. Huang, "Joint design of transmit waveform and passive beamforming for RIS-assisted ISAC system," *Signal Processing*, vol. 204, pp. 1–10, Mar. 2023.

[28] Q. Zhu, M. Li, R. Liu, and Q. Liu, "Cramér-rao bound optimization for active RIS-empowered ISAC systems," *IEEE Trans. Wirel. Commun.*, vol. 23, no. 9, pp. 11 723–11 736, Sep. 2024.

[29] Y. Wang *et al.*, "Optimizing the fairness of STAR-RIS and NOMA assisted integrated sensing and communication systems," *IEEE Trans. Wirel. Commun.*, vol. 23, no. 6, pp. 5895–5907, June 2024.

[30] M. D. Nguyen, L. B. Le, and A. Girard, "UAV placement and resource allocation for intelligent reflecting surface assisted UAV-based wireless networks," *IEEE Wirel. Commun. Lett.*, vol. 26, no. 5, pp. 1106–1110, May 2022.

[31] Y. Yu, X. Liu, and V. C. Leung, "Fair downlink communications for RIS-UAV enabled mobile vehicles," *IEEE Wirel. Commun. Lett.*, vol. 11, no. 5, pp. 1042–1046, May 2022.

[32] K. Zhao, H. Mei, S. Lyu, and L. Peng, "Joint optimization of multiple UAV-mounted RISs deployment and RIS elements allocation," in *2022 13th ICTC*, Nov. 2022, pp. 1193–1197.

[33] D. Wang *et al.*, "Active aerial reconfigurable intelligent surface assisted secure communications: Integrating sensing and positioning," *IEEE J. Sel. Areas Commun.*, vol. 42, no. 10, pp. 2769–2785, Oct. 2024.

[34] X. Chen, X. Cao, L. Xie, and Y. He, "DRL-based joint trajectory planning and beamforming optimization in aerial RIS-assisted ISAC system," in *Proc. IEEE iWRF&AT*, Shenzhen, China, Jul. 2024, pp. 510–515.

[35] A. Khalili *et al.*, "Efficient UAV hovering, resource allocation, and trajectory design for ISAC with limited backhaul capacity," *IEEE Trans. Wireless Commun.*, vol. 23, no. 11, p. 17635–17650, Sep. 2024.

[36] A. Khalili, A. Rezaei, D. Xu, and R. Schober, "Energy-aware resource allocation and trajectory design for UAV-enabled ISAC," in *Proc. IEEE Global Commun. Conf.*, Kuala Lumpur, Malaysia, Dec. 2023, pp. 4193–4198.

[37] C. Deng, X. Fang, and X. Wang, "Beamforming design and trajectory optimization for UAV-empowered adaptable integrated sensing and communication," *IEEE Trans. Wireless Commun*, vol. 22, no. 11, pp. 8512–8526, Nov. 2023.

[38] S. Sun *et al.*, "Propagation path loss models for 5G urban micro-and macro-cellular scenarios," in *Proc. IEEE 83rd Veh. Technol. Conf*, May 2016, pp. 1–6.

[39] J. Ye *et al.*, "Energy efficiency optimization in active reconfigurable intelligent surface-aided integrated sensing and communication systems," *IEEE Trans. Veh. Technol.*, pp. 1–16, Sep. 2024.

[40] J. Xu *et al.*, "Anti-jamming design for integrated sensing and communication via aerial IRS," *IEEE Trans. Commun.*, vol. 72, no. 8, pp. 4607–4619, Aug. 2024.

[41] Z. Yang *et al.*, "Secure integrated sensing and communication systems assisted by active RIS," *IEEE Trans. Veh. Technol.*, vol. 73, no. 12, pp. 19 791–19 796, Dec. 2024.

[42] R. Zhang *et al.*, "A joint UAV trajectory, user association, and beam-forming design strategy for multi-UAV-assisted ISAC systems," *IEEE Internet Things J.*, vol. 11, no. 18, pp. 29 360–29 374, Sep. 2024.

[43] D. Xu *et al.*, "Resource allocation for IRS-assisted full-duplex cognitive radio systems," *IEEE Trans. Commun.*, vol. 68, no. 12, pp. 7376–7394, Dec. 2020.